STRUCTURAL ANALYSIS METHODS TO ACCOUNT FOR MANUFACTURING DEFECTS IN COMPOSITES

Andrew Makeev*, Guillaume Seon, Yuri Nikishkov, Erian Armanios
Department of Mechanical and Aerospace Engineering
University of Texas at Arlington, Arlington, Texas, U.S.A.

Abstract

Advanced structural analysis methods that account for manufacturing defects in composite parts are needed to enable accurate assessment of their capability and useful life and enhance current design and maintenance practices. The defects must be accurately measured and the measurements must be converted into structural models to assess the effects of the defects on strength and fatigue behavior. In particular, wrinkles and porosity/voids are typical defects in carbon/epoxy and glass/epoxy composite aircraft fatigue-critical, flight-critical components. The authors overview their most recent results in the development of a comprehensive structural analysis methodology based on non-destructive detection and finite element modeling of the defects in composite specimens. Failure predictions and subsequent test correlations for composite articles with porosity/voids are presented.

1. INTRODUCTION

Advanced structural analysis methods that account for manufacturing defects in composite parts are needed to enable accurate assessment of their capability and useful life and enhance current design and maintenance practices. The defects must be accurately measured and the measurements must be converted into structural models to assess the effects of the defects on strength/fatigue behavior. In particular, the effects of inadequate design method and manufacturing process used to produce carbon/epoxy and glass/epoxy composite aircraft fatigue-critical, flight-critical components typically manifest themselves wrinkles and porosity/voids, and such defects impact the performance and the service life of these components. Recent advances in high-resolution non-destructive evaluation (NDE) methods such as 3D X-ray Computed Tomography (CT) lead to qualitative change in defect analysis methods by allowing automatic detection of various defects in composites and transition of the defect information into of structural analysis models [1-2].

The main objective of this work is to inform the engineering community about advanced structural methods and prognostics that could account for voids/porosity defects in composites and enable accurate assessment of their performance. The first technical challenge is the ability to measure the defects in three dimensions and the automated interpretation of the nondestructive measurement of defects required for accurate structural diagnostics. It is worth noting that rudimentary tools such as a ruler or a caliper could result in unacceptable measurement variation and affect the objectivity at making disposition decision of the affected part. The second technical challenge is the development of structural methods able to utilize the results of NDE in a failure prognosis that captures multiple failure modes in composite structure. The authors overview their most recent results in the development of a comprehensive structural analysis methodology based on non-destructive detection and finite element modeling of porosity/voids in composite specimens. Failure predictions and subsequent test correlations are presented.

Most of the existing works on porosity analysis in composites have been focused on attempts to relate the strength and the void volume percentage given by ultrasonic inspection [3-4]. Ref. [5] attributed scatter in strength predictions to lack of geometric and location data measurements for individual voids and used micrograph images to measure the voids. Both methods however, fail to obtain three-dimensional geometric and positional data on all sub-surface defects in the specimen.

In this work, the authors present new analysis methods based on non-destructive measurement and finite element modeling of the actual defects. Micro-focus CT is used to detect porosity defects in unidirectional IM7/8552 composite short-beam and curved-beam specimens. The specimens are subject to quasi-static loading to failure. Volume percentage of voids is calculated for all specimen scans. Analysis methods based on the global and local stress analysis of small voids are used to assess stress concentrations due to porosity/void defects. Failure criteria based on material properties obtained by the authors are used to predict failure initiation without a priori assumptions of the initial damage or the damage propagation path. Failure predictions and subsequent test correlations for

* Corresponding Author. e-mail: makeev@uta.edu.
Presented at the 38th European Rotorcraft Forum, Amsterdam, Netherlands, September 4-7, 2012.

composite test specimens with porosity/voids are presented.

Automatic detection of defects from the CT data and transition of the defect information into a finite element mesh is accomplished using image analysis software developed by the authors; and the computational models are implemented in user-defined procedures of the ABAQUS finite element software [6].

2. FAILURE PREDICTION

Structural analysis methodology presented in this work is based on the following principles:

- Microscopic damage: accounted for by material non-linear stress-strain behavior.
- Matrix-dominated failure initiation: identified using LaRC04 failure criterion based on material strength and toughness properties.
- Global model: uses stiffness degradation to account for the detected defect information included in the model. The simulation determines the critical voids that will fail first, and approximate the failure load.
- Local model for critical voids: provides more accurate failure predictions based on more accurate modeling of the detected void shape.

2.1. Material Properties

Table 1 lists stiffness and strength properties according to Ref. [7], and fracture toughness values per Ref. [8].

Table 1. Material Properties for IM7/8552 Carbon/Epoxy tape.

Tensile modulus, E_{11}	153 GPa (22.3 msi)
Tensile modulus, $E_{22}=E_{33}$	8.96 GPa (1.3 msi)
Poisson's ratio, $v_{12}= v_{13}$	0.32
Poisson's ratio, v_{23}	0.5
Shear modulus, $G_{12}=G_{13}$	5.31 GPa (0.77 msi)
Shear modulus, $G_{23}= E_{22}/(2*(1+ v_{23}))$	2.99 GPa (0.433 msi)
Secant-intercept modulus, $K_{12}=K_{13}$	260 MPa (37.8 ksi)
Secant-intercept modulus, $K_{23} = K_{12}*G_{23}/G_{12}$	147 MPa (21.3 ksi)
Exponent, n	0.203
Transverse tensile strength, Y^T	98.6 MPa (14.3 ksi)
Shear strength, S^L	113 MPa (16.4 ksi)
Mode I fracture toughness, G_{Ic}	0.2774 kJ/m^2 (1.584 psi*in)
Mode II fracture toughness, G_{IIc}	0.7889 kJ/m^2 (4.505 psi*in)

Note that secant-intercept modulus and exponent refer to approximation of the nonlinear shear stress-strain response:

$$\gamma_{ij} = \tau_{ij} / G_{ij} + \left(\tau_{ij} / K_{ij}\right)^{1/n} \quad (1)$$

2.2. Failure Initiation

Failure initiation corresponding to delamination failure is obtained from LaRC04 fracture toughness-based criterion [9]

$$\begin{aligned} &(1-g)\frac{\sigma_{33}}{S_{33}} + g\left(\frac{\sigma_{33}}{S_{33}}\right)^2 + \frac{\chi(\tau_{13})}{\chi(S_{13})} = 1, \quad \sigma_{33} > 0 \\ &\frac{\chi(\tau_{13})}{\chi(S_{13})} = 1, \quad \sigma_{33} \le 0 \end{aligned} \quad (2)$$

where $g = G_{Ic} / G_{IIc}$, and G_{Ic}, G_{IIc} are Mode I and Mode II fracture toughness values and $\chi(\tau_{13})$ is a shear component of the strain energy density

$$\chi(\tau_{13}) = 2\int \tau_{13} d\gamma_{13}(\tau_{13}) \quad (3)$$

2.3. Failure Simulation by a Global Model

Simulation of the effects and interactions of voids in the FE model of the test specimen is based on the stiffness degradation at the elements that roughly correspond to void locations. This approach has been successfully used to simulate the effect of damage due to structural failure of an element [10]. An element that overlaps a void is assumed broken. Voids that are smaller than size of an element in the fiber direction are not included in this analysis.

Failed state of a solid element for matrix-ply crack simulation assumes loss of element stiffness in the major plane of the void. CT scans of composite specimens show that voids typically have largest dimensions in the in-ply plane denoted as (1-2) plane of a specimen. A failed element loses tensile stiffness in the interlaminar material direction (3) as well as interlaminar shear stiffness in (1-3) and (2-3) planes. Failure of a significant number of elements leads to redistribution of stresses and concentration of stresses at the neighboring elements. Failure criterion (Eq. 2) is used to detect failure initiation in the specimen FE model.

2.4. Failure Simulation by a Local Model

A local model, that includes accurate void geometry obtained from CT data, is built for a critical void that is selected based on the global model prediction. The local model uses displacements from the global model as boundary conditions. A void is approximated as three-dimensional ellipse with two axis ratios provided from the analysis of two perpendicular cutting slices of the scan volume. A three-dimensional structured FE mesh is automatically built to represent void geometry using

ABAQUS scripting language. The local model provides more accurate stress calculations compared to the global model.

As adequate mesh refinement could obtain accurate converged stress concentration at the void edge, this stress is not characteristic of composite material failure due to complexity of crack initiation phenomena at the edge. Point stress and average stress methods [11] have been successfully used to detect failure based on stress fields at composite structure edges. These approaches typically use analytical stress functions or FEM stress results taken at a given characteristic distance from the stress concentration or singularity. Convergence of FEM stress results at this distance can usually be achieved within reasonable mesh refinements. Practical application of these methods is based on finding the characteristic distance and using unnotched strength properties to predict failure initiation for different coupons of the same material and geometry. This methodology has been successfully used for strength prediction of typical composite specimens with circular open holes and mechanically fastened joints [11, 12].

One of the objectives of this work was to assess the ability of these methods to provide accurate predictions for unidirectional laminates with embedded voids due to porosity. For this purpose, point-stress and average-stress approaches were adapted to the LaRC04 failure criteria given in Eq. 2. Point-stress and average-stress characteristic distances were calibrated using angle beam specimens with representative range of void geometries and test failure loads.

2.5. Analysis Algorithm

The technical approach to account for the porosity/voids manufacturing defects in the failure models is based on the following workflow:

(1) Build the FE model that does not include porosity/voids;
(2) Detect porosity/voids shapes and locations;
(3) In the FE model, mark elements corresponding to voids that overlap elements as failed;
(4) Determine the critical void that leads to failure in the global model;
(5) Build local mesh for this void geometry and apply displacement boundary conditions from global model;
(6) Use failure criteria in the local model to predict initiation of structural damage.

Combination of the global and local analysis methods is required to efficiently handle complexity and amount of porosity defects in composite parts. The global analysis method captures stress redistribution on the scale of the specimen; the local analysis method is able to resolve the stress field with the accuracy necessary for capturing the failure.

The following sections demonstrate application of this analysis to unidirectional short beam shear and curved beam specimens that represent the effect of voids/porosity on interlaminar shear and interlaminar tension failures.

3. FAILURE OF UNIDIRECTIONAL SHORT-BEAM SHEAR SPECIMEN

3.1. Defect detection in test specimens

Batches of unidirectional IM7/8552 Carbon/Epoxy 0.25 inch (6.25 mm) thick square cross-section short-beam specimens cured at three different curing pressure levels (10 psi, 14 psi and 25 psi or 69 kPa, 97 kPa and 172 kPa: batches C, B and A, respectively) resulted in varying degrees of porosity. Three specimens corresponding to each curing pressure have been loaded till shear failure. For more details on the test setup see Ref. [13].

To capture volumetric porosity data all specimens have been scanned using 225 kV X-ray Computed Tomography system manufactured by North Star Imaging Inc before structural tests were completed. The scans have been accomplished at 40 kV tube voltage and 300 µA target current at 0.45 frames per second and 12X magnification to maximize resolution for 1 inch (25.4 mm) of specimen length. This resulted in effective pixel pitch of 10 microns (0.4×10^{-3} in) and effective ability to detect voids from 30 microns (1.2×10^{-3} in) in size. Figure 1 shows typical through-the-thickness slices of the specimens of all three porosity levels.

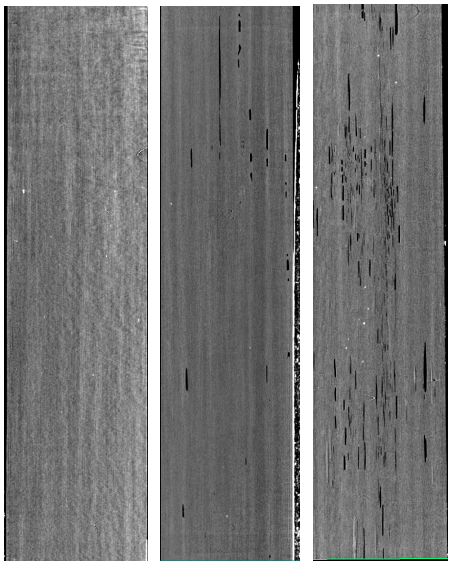

Figure 1. Typical through-the-thickness CT scan volume slices of the specimens of all 25 psi (left), 14 psi (center) and 10 psi (right) curing pressure.

Through-the-width slices of the CT scan volume have been analyzed by the porosity detection software tool. The software identified and classified voids in the CT scan volume slices and calculated total volume of porosity in the specimens. Void location and geometry data were used by user subroutine UMAT [6] in ABAQUS FE simulations. Figure 2 shows results of void identification. Blue color shows voids of the aspect ratio larger than 10, red color denotes aspect ratio smaller than 10 and yellow shows non-elliptical voids.

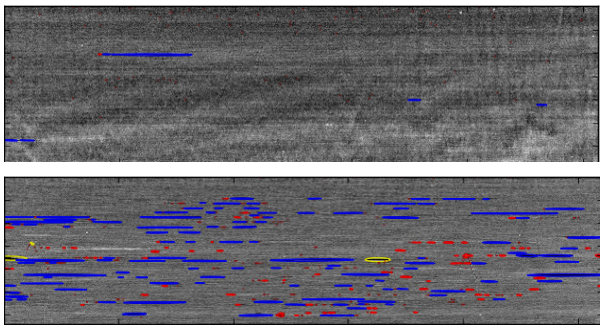

Figure 2. Identification of voids for CT scan volume slices of the specimens at 14 psi (B-3, top) and 10 psi (C-3, bottom) curing pressure.

Volume percentage of the voids is calculated based on image analysis of all slices of the CT scan volumes that included 1 inch (25.4 mm) of the specimen in length, which corresponded to an area between the supports. A pixel intensity that separated voids from material was selected from visual comparison with CT scan volume slices.

3.2. Failure load predictions by the global model

The finite element model of the SBS specimen test included frictionless contact simulation between the specimen and loading nose and supports modeled as analytical surfaces. Linear 8-noded reduced integration elements (C3D8R) were used; material behavior was defined according to Table 1 by the user subroutine UMAT.

Table 2. Simulation of porosity and test results for SBS specimens.

Specimen			Simulation		Test
No	Thickness / width, mm	Porosity volume, %	Fail. Load, kN	Error, %	Failure Load, kN
A1-A3	6.76 / 6.48 (avg)	0.01 (avg)			6.61 (avg)
B-1	6.74 / 6.41	0.064	5.7	-4.5	5.94
B-2	6.76 / 6.44	0.059	5.7	-4.5	5.94
B-3	6.78 / 6.43	0.105	6.0	-3.0	6.19
C-1	6.55 / 6.41	1.89	4.7	-8.3	5.09
C-2	6.54 / 6.41	1.21	4.3	-14.2	5.05
C-3	6.53 / 6.44	1.84	4.3	-15.8	5.15

Table 2 shows comparison of the global void analysis predictions and test results. Failure loads are compared for specimens with medium and high levels of porosity. Specimens at low porosity levels (25 psi curing pressure) have failed at the same loads as specimens without defects. The CT scans did not detect voids near these specimen mid-planes and no analysis was executed for them. For most of the specimens locations of the voids were also predicted correctly; errors increased as void percentage increased.

Note that in the areas of void concentrations, local percentage of porosity can be significantly higher than reported in Table 2.

Figure 3 shows LaRC04 failure index values at failure for specimens with porosity. Same through-the-width sections as in Figure 2 are displayed. Light grey colors show failure locations. Voids appear as solid blue areas; values of failure index at element integration points are displayed. Note that the failure locations under the loading nose and above the supports are ignored due to incorrect predictions of failure criterion under transverse compressive loads.

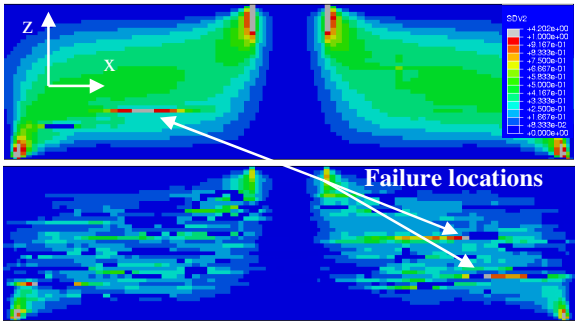

Figure 3. Failure index for through-the-width slices of the specimens at 14 psi (B-3, top) and 10 psi (C-3, bottom) curing pressure.

The above simulations used 20 slices of the CT scan volume out of 600 total slices available at the scan resolution. The number of slices corresponds to the number of elements through the model width; this number resulted in size of FE models that took about 1 hour to execute on six 2.66 GHz Intel Xeon ® processor cores. The number of slices needed for the analysis depends on the size of defects in the width direction. Figure 4 shows typical cross-sectional slices for specimens with medium and high porosity levels; through-the-width sizes of voids range from 100 to 300 microns (4 to 12×10^{-3} in).

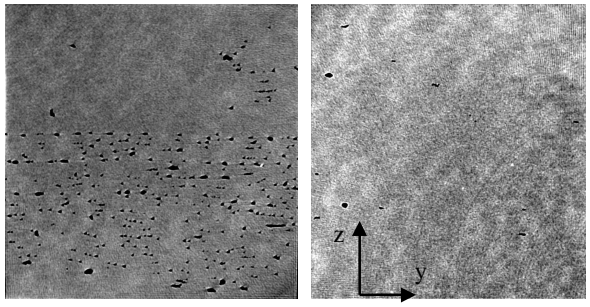

Figure 4. Typical cross-sectional slices of the specimens at 14 psi (left) and 10 psi (right) curing pressure.

The simulations based on global void analysis demonstrated qualitative correlation of failure loads and locations of delaminations in unidirectional short-beam shear specimens with two levels of porosity. Tests demonstrated relatively small effects of porosity on interlaminar shear-dominated failure: the specimens with large porosity volume percentage (around 2% total volume) have shown about 20% of strength knock-down on average. Local analysis was not performed for these specimens due to good quality of global model predictions.

4. FAILURE OF UNIDIRECTIONAL CURVED-BEAM SPECIMEN

4.1. Defect detection in test specimens

Two batches of unidirectional IM7/8552 Carbon/Epoxy 0.25 inch (6.25 mm) thick and 0.5 inch (12.5 mm) deep curved-beam specimens with the internal radius of 0.25 inch (6.25 mm) were cured at three different curing pressures: 80 and 100 psi (552 and 689 kPa), batches E and F, respectively. Specimens from each batch have been loaded until failure. For more details on the test setup see Ref. [13].

To capture volumetric porosity data all specimens have been scanned using a 225 kV micro-focus CT system manufactured by North Star Imaging Inc before structural test was done. The scans were accomplished at 40 kV tube voltage and 400 μA target current at 0.5 frames per second and 10.5X magnification to maximize resolution for the curved part of the specimen. This resulted in effective pixel pitch of 12 microns (0.5×10^{-3} in) and effective ability to detect voids from 36 microns (1.5×10^{-3} in) in size.

Batch E cured at 80 psi curing pressure was initially intended to be used as reference specimens free of defects, to be compared with the high porosity content batch. However, large scatter in the interlaminar strength shown by the test data validated the detailed NDE of batch E by X-ray tomography. The scans detected few voids but some of these voids had significant length and were located in the area of interlaminar tensile stress concentration. Although the porosity volume percentage was small (0.05-0.1% of the full volume of the scans shown on Figs. 5-6), the size of the voids resulted in large strength degradation. Figure 5 shows the largest voids discovered in the two sample coupons from batch E, their strength knock-downs and defect sizes.

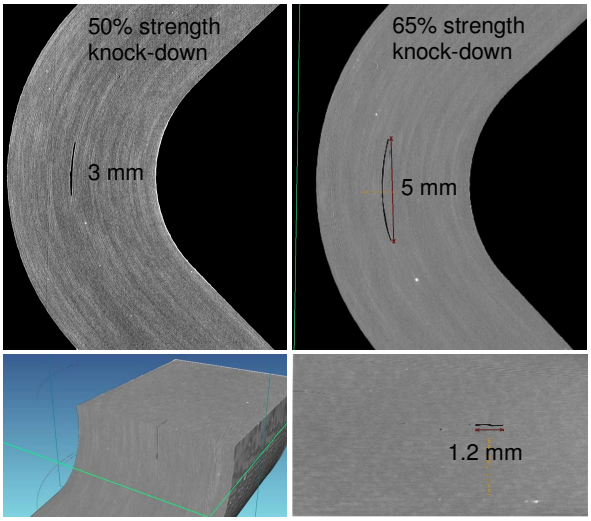

Figure 5. Cross-sectional slices of the two coupons from batch E (top) and through-the-thickness geometry of the voids (bottom).

Figure 6 demonstrates failure patters in failed curved beam specimens from batch E. The Figure suggests that crack initiates from a single largest void in the area of interlaminar stress concentration in the middle of the curved part. Voids that have largest aspect ratios in the fiber direction lead to maximal strength degradation, which is intuitively sound.

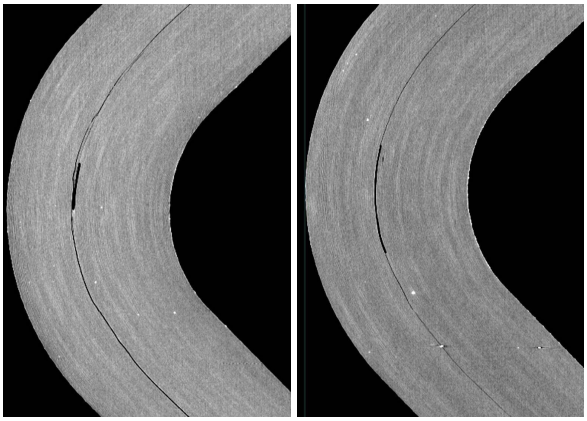

Figure 6. Cross-sectional slices of the two failed coupons from batch E.

Void thickness was found to be almost constant and the smallest of the three dimensions used to characterized the void by a three-dimensional ellipse. This pattern is a consequence of the void formation mechanism. Expansion of air pockets encounters the largest resistance in the thickness direction, due to application of autoclave pressure.

4.2. Failure predictions by the global model

The finite element model of the curved beam specimen test was built. The model used frictionless contact definition between the specimen and 0.75 in (19 mm)-diameter rollers modeled as analytical surfaces. Linear 8-noded reduced integration elements (C3D8R) were used; material behavior was defined according to Table 1 by the user subroutine UMAT.

Through-the-width slices of the CT scan volumes of the specimen curved part have been analyzed by the void analysis software described in the previous section. All slices have been used for void analysis; 12 micron (0.5×10^{-3} in) resolution led to about 1000 slices for the 0.5 in (12.7 mm) specimen width.

The void slices identified by the software and approximated as ellipses were then intersected with the elements of the global FE model to identify failed elements. The stress analysis used LaRC04 index (Eq. 2) to identify location of the critical voids and failure loads. Table 3 details the results of this analysis for coupons from batches E and F.

Table 3. Global model failure predictions.

Specimen		Simulation		Test
No	Thickness mm	Failure Load, kN	Error, %	Failure Load, kN
E-16	6.76	1.2	29	0.93
E-17	6.73	1.6	-14	1.85
F-1	6.60	1.5	-25	2.00
F-2	6.67	1.5	-39	2.47
F-3	6.68	1.8	-27	2.45
F-4	6.68	0.9	-56	2.06

Due to significant errors in failure loads, a local analysis of critical voids was deemed necessary. Results of global analysis were used to identify critical voids and provide initial estimation of the failure load for local analysis. The local analysis models used CT scan geometric data for critical voids. Predictions of local analysis models are described in the next section.

4.3. Failure load predictions by the local model

Four specimens from batch E were selected to calibrate the characteristic distance for point stress and average stress methods. Locations and geometries of these voids were used to build local FE sub-models. Specimens were selected in order to ensure a representative range of the void geometries typically observed. Table 4 provides test failure loads and aspect ratios of the voids selected in the calibration specimens.

Table 4. Failure loads and void geometry for calibration specimens.

Specimen No	Failure load, kN	Thickness mm	Aspect ratio fiber dir.	Aspect ratio width dir.
E-14	2.61	0.089	10.1	4.4
E-15	1.27	0.089	37.6	3.0
E-16	0.93	0.089	81.2	5.0
E-17	1.85	0.089	25.3	4.7

FE local submodels for each failure void were built as illustrated on Figure 7. Curvature of the plies and local material orientation was taken into account. Linear 8-noded hexagonal 3D elements C3D8R with reduced integration scheme were used in the model. Typical total number of degrees of freedom was in the 500,000 – 800,000 range.

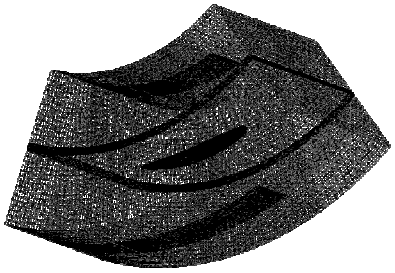

Figure 7. 3D hexagonal mesh for local model of failure void.

Adequate mesh refinements were defined around the void and convergence of local stresses was verified. Displacements from the global model were applied as boundary conditions for the six faces of the submodel volume. For each specimen, the global model solution was obtained at failure load given by test data.

Stress field in the curved area of the angle beam is dominated by the interlaminar tensile stress. Tensile stress concentration develops at the edge of the void, along the longest dimension (fiber direction) and in the plane of the ellipse minor radius cross section, as illustrated in Figure 8. Maximum concentration is found at about mid length of the void. LaRC04 failure index is plotted in the maximal failure plane as a function of the distance to the void edge along short ellipse axis. Typical spatial distribution of the damage index is illustrated on Figure 9.

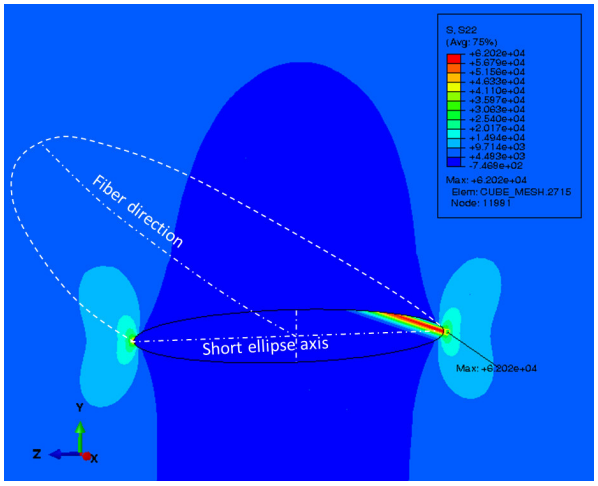

Figure 8. FE local model tensile stress concentration at void edge.

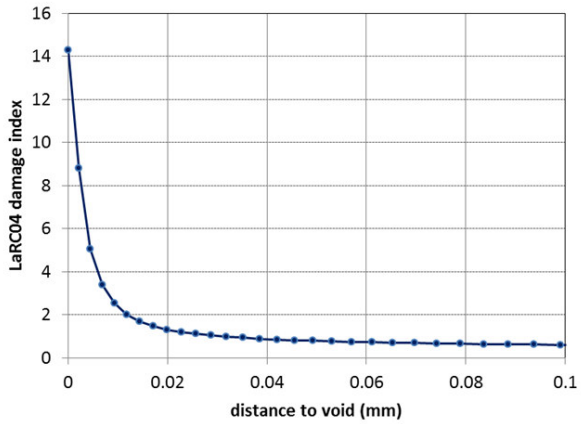

Figure 9. Damage index versus the distance from the void boundary and along the minor ellipse axis.

Characteristic distance for the point stress method was defined as the distance at which the LaCR04 damage index is equal to one, when failure load is applied. Average-damage approach is also derived from the average-stress method [11]. The average damage index defined in Eq. 4 is computed along the short ellipse axis in the cross-section plane with maximum damage.

$$D_{av} = \frac{1}{x}\int_0^x D(r)dr \quad (4)$$

D is the LaRC04 damage index defined in Eq. 2 and *x* the distance to void boundary. The characteristic distance is defined as the distance at which the average damage is equal to one at failure load.

LaRC04 damage index field is computed at material points using the state variable defined in the ABAQUS UMAT user subroutine. Results are post-processed along the path defined by the short ellipse axis. Characteristic distances for point stress and average damage approaches are listed in Table 5.

Table 5. Point stress and average damage characteristic distance for calibration specimens.

Specimen No	Point stress distance, mm	Average damage distance, mm
E-14	0.034	0.153
E-15	0.027	0.126
E-16	0.029	0.163
E-17	0.035	0.157
deviation	0.003	0.014
average	0.031	0.150

The characteristic distance for both point and average stress methods is not a material constant and depends on hole geometry and laminate stacking sequence [11]. However, Table 5 shows relatively small scatter in the characteristic distances. The following analysis demonstrates that the average distance calibrated at 0.031 mm (1.23×10^{-3} in) and 0.15 mm (5.90×10^{-3} in) for point stress and average damage methods, respectively, can be used in a failure prediction procedure for specimens with various void geometries and positions. Figure 10 shows dependency of the point stress characteristic distance with respect to the applied load. A linear dependence is illustrated, with a trend to a stiffer slope for specimens with lower failure loads. The average damage approach leads to similar results.

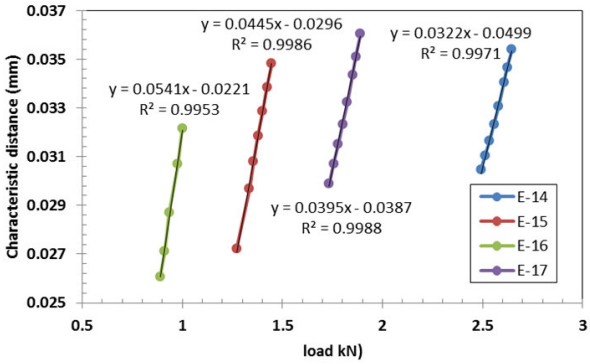

Figure 10. Changes in point stress characteristic distance with the applied load.

These observations suggested the following procedure for failure load predictions using the local model:

(1) Use the global model to determine the defect that leads to failure and predict the initial approximation for the failure load;
(2) Build the local model for the critical void and use the displacement boundary conditions from the global model;

(3) Run the global and the local models with the sub-model boundary conditions for another load value (90% to 110% of the failure load approximation) to determine the linear relationship between the applied load and the characteristic distance (see Figure 11) for the point-stress and average-damage methods.
(4) Update the failure load using the calibrated 0.031 mm (1.23×10^{-3} in) point-stress characteristic distance, and 0.15 mm (5.90×10^{-3} in) average-damage characteristic distance;
(5) Run the global and the local models for the failure load approximation calculated in the previous step; and extract the point-stress and the average-damage characteristic distances to compare with the calibrated values;
(6) Repeat steps 3 to 5 till convergence in the characteristic distance is established (2% error limit used in this work.) Multiple iterations are frequently required due to nonlinear load-displacement relations (geometric nonlinearity) in the curved-beam specimens.

This procedure was validated for the 4 calibration specimens. Failure loads obtained are compared with test results in Table 6.

Table 6. Failure load predictions for calibration specimens.

Spec. No	Test failure load, kN	Point stress		Average damage	
		Failure load, kN	Error, %	Failure load, kN	Error, %
E-14	2.61	2.52	-3.4	2.59	-0.5
E-15	1.27	1.37	6.8	1.37	7.1
E-16	0.93	0.99	5.4	0.90	-3.4
E-17	1.85	1.76	-5.1	1.81	-2.0

FE local model results correlate well with test data, which validates the prediction procedure. A maximum relative error of 6.8% and 7.1% for point stress and average damage method is reported, respectively. The average error is 5.2% for the point stress method and 3.3% for the average damage approach. This demonstrates that despite the scatter in characteristic distances, a single average value can be efficiently used in this case and provides accurate predictions. For all the specimens, failure is dominated by the interlaminar tension that initiates along the long edge of the void.

Proposed analysis procedure was verified on the specimens with different void geometries and porosity volume content. Failure load predictions were obtained for 5 specimens from batch E (80 psi curing pressure) and two specimens from batch F (100 psi curing pressure). Table 7 compares FE local model predictions with test results.

Table 7. Failure load predictions for validation specimens.

Spec. No	Test failure load, kN	Point stress		Average damage	
		Failure load, kN	Error, %	Failure load, kN	Error, %
E-1	2.24	2.18	-2.7	1.98	-12.8
E-2	1.34	1.37	1.9	1.35	0.3
E-3*	1.29	1.11 [1.62]	-15.6 [20.8]	1.22 [1.79]	-5.5 [28.3]
E-4	1.89	1.83	-3.4	1.99	5.1
E-5*	1.86	1.81 [2.26]	-2.7 [17.7]	1.63 [1.98]	-14.5 [5.6]
F-2	2.47	2.39	-3.4	2.53	2.3
F-3	2.45	2.52	2.8	2.52	2.8

* Conservative predictions were obtained by merging the nearby voids on the crack plane. Predictions for a single void are listed in brackets.

Good correlation with experimental data is demonstrated for validation specimens from batches E and F as shown in Table 7. Excellent agreement with tests is found for specimens F-2 and F-3 from batch F (100 psi curing pressure). For batch E specimens (80 psi curing pressure), in the analysis of a single critical void maximum relative error is obtained for specimen E-3: 20.8% and 28.3% relative error for point-stress and average-damage methods, respectively. Specimen E-5 also shows large relative error (17.7%) for the point stress method. Inspection of the CT scans after failure revealed the presence of two closely located voids along the crack line: in the cross-sectional plane for E-3 and in the through-the-width plane for specimen E-5. This is illustrated on Figure 11.

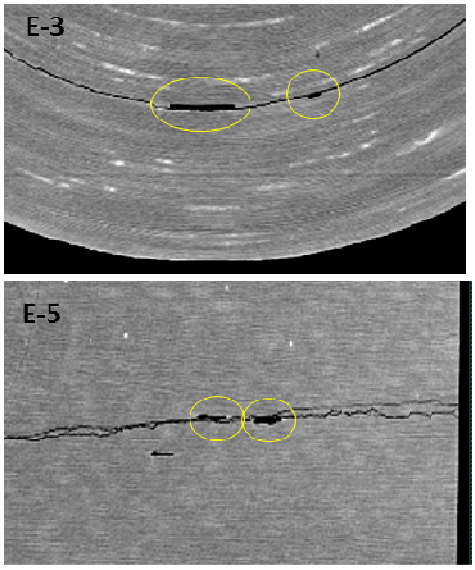

Figure 11. Samples of closely located voids in the same crack plane for batch E specimens.

This pattern was not observed in the other specimens, in which a single void was detected on the crack. The local method only considers one void and the largest void was selected for construction of E-3 and E-5 FE local meshes. In both cases, single void predictions resulted in higher failure load values, which is consistent with the larger strength degradation due to contribution of several voids. A conservative approach was adopted by merging the voids identified in Figure 11 into a single void of the equivalent total length. Conservative results were obtained and better agreement with test results is reported for these cases in Table 7.

The prediction method based on local model analysis demonstrated the ability to obtain accurate results for specimens where interaction between voids is negligible. It can be successfully applied to cases with relatively low porosity content. The method highlights the critical importance of void geometry and its effect on strength degradation. Even if small global percentage of porosity is reported, a single void with high aspect ratio can lead to stress concentrations and early initiation of delamination. High resolution three-dimensional NDE methods are required to obtain accurate geometry dimensions of voids and automatic geometry extraction methods are needed to build high fidelity local FE models.

More effort is required for accurate prediction of failure in specimens with high porosity content. Selection of the critical void for local model analysis becomes a difficult task, and interaction between voids cannot be neglected as many voids are located closely on the failure plane. Merging the voids to achieve conservative predictions is a viable strategy that however requires extensive technical effort to verify and is currently in progress. Techniques that use super-elements, fracture mechanics and cohesive element-based methods are also investigated by the authors.

5. CONCLUSIONS

Manufacturing defects can severely deteriorate the matrix-dominated properties resulting in degraded strength and fatigue structural performance of composites. Although it might not be practical to eliminate all the defects in a composite part, it is possible to avoid assumptions of the worst-case scenario and address improved part durability and damage tolerance once the defects and their effects are captured. Advanced technology to measure the defects and understand their effects on structural performance could potentially enable a fundamental shift to accurate assessment of condition for composite parts. Our goal is to develop such technology and make it the industry standard practice for structural diagnostics in the existing and the emerging composite aircraft platforms.

In this work we demonstrated that (1) accurate three-dimensional non-destructive measurement of porosity/voids defect location and size can be achieved using CT based technologies; and (2) structural analysis models built based on automatic transition of the defect information into a finite element mesh lead to accurate characterization of the effects of the defects. The methodology and models demonstrated on relatively simple material scale composite test articles show that current accept/reject criteria based on the defect volume percentage approximations in the part volume are not adequate. That is a single defect present at the critical location could be more harmful than multiple defects present throughout the part. In particular, it was demonstrated that specimens with low porosity content (about 0.1% volume) were susceptible to large strength degradation (more than 50%) for a single void located in the critical area.

The measurement techniques and analysis methods must focus on critical locations prone to failure to enable accurate assessment of part condition. Accordingly, accurate three-dimensional measurement of defect location and size; and ability of structural analysis techniques to capture complex failure mechanisms are a key to successful structural diagnostics and failure prognosis for composite structures.

ACKNOWLEDGMENTS

This work is sponsored by the Office of Naval Research. Such support is gratefully acknowledged. The views and conclusions contained in this article should not be interpreted as representing the official policies, either expressed or implied, of the U.S. Government.

The authors also would like to thank Mr. Ed Lee (Bell Helicopter Textron) for manufacturing the specimens used in this work; and Mr. Luca Airoldi, Dr. Yihong He and Mr. Brian Shonkwiler (University of Texas at Arlington) for their assistance with CT scans, creating FE models and specimen testing, respectively.

REFERENCES

[1] Makeev, A., Nikishkov, Y., Carpentier, P., Lee, E., and Noel, J. “Manufacturing issues and measurement techniques for assessment of the effects on structural performance of composite parts,” *Proceedings of the AHS 66th Annual Forum*, Phoenix, AZ, 2010.

[2] Makeev, A., Nikishkov, Y. “Fatigue Life Assessment for Composite Structure,” *Proceedings of the 26th ICAF Symposium*, Montréal, Canada, 2011.

[3] Almeida, S. F. M., and Neto, Z. S. N., “Effect of void content on the strength of composite laminates,” *Composite Structures,* Vol. 28, 1994, pp.139-142.

[4] Costa, M. L., and Almeida, S. F. M., “The influence of porosity on the interlaminar strength of carbon/epoxy and carbon/bismaleimide fabric laminates,” *Composite Science and Technology,* Vol. 61, 2001, pp. 2101-2108.

[5] Huang, H., and Talreja, R., “Effect of void geometry on elastic properties of unidirectional fiber reinforced composites”, *Composite Science and Technology,* Vol.65, 2005, pp.1964-1981.

[6] ABAQUS 6.11.1. User’s Manual, ABAQUS Inc., Pawtucket, RI, USA, 2011.

[7] Makeev, A., Seon, G., and Lee, E., “Failure Predictions for Carbon/Epoxy Tape Laminates with Wavy Plies,” *Journal of Composite Materials*, Vol. 44, 2010, pp. 95-112.

[8] Camanho, P. P., and Lambert, M., “Design methodology for mechanically fastened joints in laminated composite materials,” *Composites Science and Technology*, Vol. 66, 2006, pp. 3004–3020.

[9] Davila, C. G., Camanho, P. P., and Rose, C. A., “Failure Criteria for FRP Laminates,” Journal of Composite Materials, Vol. 39, 2005, pp. 323–345.

[10] Nikishkov, Y., Makeev, A., and Seon, G., “Simulation of Damage in Composites based on Solid Finite Elements,” *Journal of the American Helicopter Society*, Vol. 55, 042009, 2010.

[11] Whitney, J. M., and Nuismer R. J., “Stress fracture criteria for laminated composites containing stress concentrations,” *Journal of Composite Material*s, Vol. 8, 1974, pp. 253–65.

[12] Camanho, P. P., and Lambert, M., “Design methodology for mechanically fastened joints in laminated composite materials,” *Composites Science and Technology*, Vol. 66, 2006, pp. 3004–3020.

[13] Makeev, A., He, Y., Shonkwiler, B., Lee, E., Nikishkov, Y., “A Method for Measurement of Three-Dimensional Constitutive Properties for Composite Materials,” *Proceedings of the 18th ICCM*, Jeju, Korea, 2011.